Effect of Spacecraft Charging on Performance of Ion Electrospray Propulsion Systems

75th International Astronautical Congress (IAC), Milan, Italy, 14-18 October 2024.

IAC–24–C4.5.4

Effect of Spacecraft Charging on Performance of Ion Electrospray Propulsion Systems

Saba Z. Shaik[a*], **Matthew N. Corrado**[b], **Paulo C. Lozano**[c]

[a] *Ph.D. Candidate, Department of Aeronautics and Astronautics, Massachusetts Institute of Technology., sshaik@mit.edu*
[b] *Ph.D. Candidate, Department of Aeronautics and Astronautics, Massachusetts Institute of Technology., mcorrado@mit.edu*
[c] *Professor, Department of Aeronautics and Astronautics, Massachusetts Institute of Technology., plozano@mit.edu*
[*] *Corresponding author*

Abstract

Ion electrospray propulsion systems are known to induce moderate levels of spacecraft charging when operated in a passive dual-polarity neutralization scheme. Here, the relationship between this charging and the performance of the electrospray thrusters is experimentally assessed. We characterize a passively-fed ion electrospray thruster in a simulated spacecraft charging environment with the ionic liquid propellant EMI-BF_4. Performance metrics, including thrust, specific impulse, and component efficiencies are estimated with the thruster operated at emission currents of ± 150 µA for prescribed spacecraft biases between 0 and ± 800 V. When the spacecraft and plume are the same polarity, thrusters exhibit a narrower plume and produce more thrust with increasing spacecraft bias. Conversely, when the spacecraft and plume are opposite polarities, thrusters show increasingly divergent plumes that are attracted back to the spacecraft, resulting in less thrust being produced at higher spacecraft biases. The combined thrust output for a dual-polarity pair of thrusters was estimated to decrease by about 36% at a spacecraft bias of 800 V and 25% at a spacecraft bias of −800 V. These results show that spacecraft charging is a critical consideration for determining the true in-space performance of ion electrospray propulsion systems.

Nomenclature

F	=	thrust, corrected [µN]
F_{ToF}	=	thrust, uncorrected [µN]
I_{em}	=	emitted current [µA]
I_{ex}	=	intercepted current [µA]
I_{sp}	=	specific impulse [s]
$\dot{m}$	=	mass flow rate, corrected [µg/s]
$\dot{m}_{ToF}$	=	mass flow rate, uncorrected [µg/s]
η_E	=	energy efficiency
η_R	=	return efficiency
η_p	=	polydispersive efficiency
η_T	=	total efficiency
η_θ	=	angular efficiency
η_{tr}	=	transmission efficiency
q	=	particle charge [C]
V_0	=	applied emitter potential [V]
V_{ex}	=	applied extractor potential [V]
V_{RP}	=	retarding potential [V]
V_{SC}	=	spacecraft potential [V]
V_{th}	=	extraction voltage [V]

1. Introduction

The need for small yet agile spacecraft has steadily increased as a result of the emergence of a new generation of space missions and space-enabled technology characterized by large numbers of extremely capable space-based platforms cooperating to serve a shared purpose. A key enabling technology for these highly precise and mobile platforms is compact and efficient propulsion systems. Electrospray thrusters represent a form of in-space electric propulsion unique in its ability to provide efficient and precise thrust using moderate levels of power and nontoxic vacuum-stable propellants [1]. Despite these benefits, a unique challenge to implementing electric propulsion systems is the complex phenomenon of spacecraft charging. Because most electric propulsion systems produce exhaust beams charged to a single polarity (usually positive ions for plasma-based thrusters), intentional measures must be taken to prevent the buildup of a significant nonzero charge on the spacecraft, which is accomplished by maintaining a net zero current into and out of the spacecraft at all times. Plasma thrusters emitting positively-charged beams typically utilize external cathodes serving as electron emitters to maintain this neutrality, but this comes at a cost of mass, volume, and often power and/or propellant consumption, these drawbacks being significant for compact systems such as electrospray thrusters. Additionally, electron-based neutralizers are unable to neutralize negatively-charged beams which can be produced by ionic liquid electrospray thrusters.

An advantage of electrospray thrusters is their ability to produce either positive or negative ion beams, so electrospray thruster heads are typically operated in pairs in a dual-polarity configuration, with one thruster emitting

a positive beam current $+I$ and the other a negative current $-I$, thus producing, ideally, a globally neutral beam if the positive and negative emitted currents are perfectly matched. Additionally, the polarity of the ion beam is periodically reversed to avoid electrochemical degradation of the ionic liquid propellant [2]. This setup is shown in Figure 1. Though coming with the penalty of requiring duplicate electronic circuits and propellant feed systems to accommodate the need for simultaneously operating in both polarities, this penalty can be much less significant than other neutralization techniques that make no contribution to thrust [3, 4]. While perfect in theory, real operation of bipolar thruster pairs can still result in spacecraft charging because even minute imbalances in emitted current can yield relatively large changes in electric potential due to the usually small self capacitance of a spacecraft [5]. It is also common for spacecraft charging to occur due to external factors, such as ambient space plasma or solar wind [6]. Because some degree of spacecraft charging is at worst inevitable and at best a possibility, it is vital to understand how the phenomenon impacts critical spacecraft systems such as the propulsion system itself. While previous studies have investigated the effect that thruster operation has on the spacecraft potential [5, 7, 8], there is little existing work focused on quantifying the effect that the resulting spacecraft potential has on thruster performance. Clearly, the operation of an electric propulsion system and the electric charge of the spacecraft are highly coupled, so it is imperative to characterize all the relevant cause-and-effect relationships in order to fully understand the phenomena and design spacecraft and missions around them.

Here we characterize the impact that spacecraft charging has on the performance of a notional electrospray propulsion system, in particular focusing on the effective thrust of the system as a function of spacecraft potential. The charged spacecraft scenario is experimentally simulated in a vacuum chamber environment with a version of the MIT ion electrospray propulsion system (iEPS) as the thruster system. We will compare our results to previously proposed models for the effect of spacecraft charging on thrust to determine the relative significance of various factors in the overall impact to thruster performance.

2. Background

2.1 Passive Charge-Balancing Mechanisms

Passive means of spacecraft neutralization are of interest to preserve the advantages in size, weight, and power that electrospray propulsion systems offer. Two key passive mechanisms regulate the level of spacecraft charging induced by electrosprays operated in a dual-polarity scheme. The first is the use of galvanic isolation in the thruster's power processing unit (PPU), detailed more in Ref. [5] and shown in Figure 2. The emitters are connected in series with their extractors grounded to the spacecraft. The high voltage power supply remains floating and is isolated from the spacecraft ground through the capacitor C_{HV}, forcing the currents emitted by the thruster heads to be equal in magnitude. For example, if thruster B emits slightly more current than thruster A, a positive potential difference $V_{HV,GND}$ forms across the capacitor. This results in the extraction voltage for thruster A increasing, thus causing it to emit more current, while the opposite occurs for thruster B. Eventually, an equilibrium state is reached where the emitted currents I_A and I_B are equal, $V_{HV,GND}$ is nonzero, and the spacecraft potential is stable.

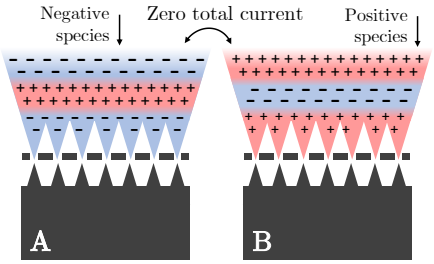

Fig. 1. Periodic polarity alternation for a dual-polarity pair of electrospray thrusters.

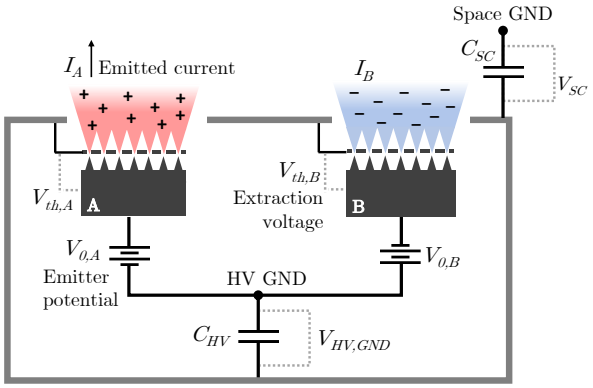

Fig. 2. Diagram of galvanic isolation in the PPU design employed for dual-polarity iEPS operation.

Although this strategy successfully constrains the emitted currents for a pair of thrusters to be equal, there is no way to ensure that the intercepted currents are perfectly matched. Intercepted current refers to the portion of the emitted current that impinges on the extractor grid. Due to minor variations in the microfabrciation processes and as-

sembly of the thrusters, each thruster head has slightly different I-V characteristics. This results in unavoidable differential interception between pairs of thrusters, and thus a finite net current is emitted from the spacecraft. Due to the low self-capacitance of conductive spacecraft bodies, even vanishingly small net currents will induce significant spacecraft charging.

Fortunately, this charging is bounded by the thrusters' "return current" [5, 7], a second passive charge-balancing mechanism. Electrospray plumes are polydisperse and always feature a low-energy population of ions due to cluster fragmentation events and other energy losses [9]. If a spacecraft charges to a potential V_{SC}, any emitted particles that posses a kinetic energy less than qV_{SC} will be attracted back to the spacecraft and deposit their charge, thus contributing no net current flux. This return current ensures that the spacecraft will never charge to a potential greater than the thruster's firing potential, especially in the dual-polarity scheme [5]. Of course, the return current also constitutes a performance loss since any particles that arrive back at the spacecraft produce no net thrust.

2.2 Effect of Charging on Thrust

Spacecraft charging is expected to affect the thrust output of an electrospray system through changes in the composition and structure of the emitted ion beam. These effects have not yet been experimentally assessed due to the difficulty of performing simultaneous thrust and spacecraft charging measurements in a laboratory environment. The factors that are anticipated to most significantly impact thrust are discussed in this section.

Mier-Hicks estimates the effect of emitter potential on thrust output [5]. The ratio of the combined thrust output of a dual-polarity pair of electrospray thrusters on a charged spacecraft (F_*) and noncharged spacecraft (F) is given in Equation 1. Here, V_{SC} is the spacecraft potential, and $V_{th,A}$ and $V_{th,B}$ are the extraction voltages (i.e. difference between emitter and extractor potentials) for each thruster as indicated in Figure 2. In a noncharging scenario, the total thrust output is twice that of a single thruster. When V_{SC} is nonzero, one ion beam is decelerated by the spacecraft while the other is accelerated. The thrust then deviates from its nominal value with a square-root dependence on the spacecraft potential. In a worst case scenario where the spacecraft is fully charged to the thrusters' extraction potential, the combined thrust penalty should be just 30%.

$$\frac{F_*}{F} = \frac{\sqrt{1+\frac{V_{SC}}{V_{th,A}}}+\sqrt{1+\frac{V_{SC}}{V_{th,B}}}}{2} \qquad [1]$$

While this model provides insight into the dependence of thrust on voltage, it does not account for other losses that may be important. The return current, which can be present when V_{SC} is nonzero, contributes no net thrust. Additionally, electrostatic forces from the charged spacecraft will likely alter the structure and velocity distribution of the thruster's plume, potentially increasing beam divergence losses at high spacecraft potentials. For instance, a positive particle emitted at the plume's periphery will experience acceleration back toward a negatively-charged spacecraft, increasing its half-angle with respect to the thruster centerline. Since the horizontal component of the particle's velocity does not produce thrust (assuming an axisymmetric current distribution), this change in trajectory results in thrust loss.

While it is possible that spacecraft charging may create other types of performance losses, the aforementioned are expected to be the most significant. In this work, we aim to measure each of them and determine how they evolve with increasing spacecraft potential. These results will serve to provide a more realistic picture of in-space thruster performance.

3. Methods

The ion electrospray propulsion system (iEPS) developed at MIT was used for all experiments in this work. iEPS is a microfabricated, passively-fed electrospray thruster whose emitter array consists of 480 individual tips patterned on a porous borosilicate glass substrate. The extractor electrode, fabricated from silicon and coated in gold, is manually aligned and bonded to the emitter. The thruster head is mounted onto a porous Teflon propellant reservoir with a capacity of about 1 mL. The reservoir is housed within a PEEK shell that provides structural support and an interface to the circuit board used in laboratory testing. For propellant, the ionic liquid 1-ethyl-3-methylimidazolium tetrafluoroborate (EMI-BF_4) was chosen as it is commonly used and its emission characteristics are generally well-understood for electrospray propulsion systems. The iEPS unit used in these experiments is shown in Figure 3. Mier-Hicks measured induced spacecraft potentials in the range of $\pm$ 200 V for a similar thruster [5]. More details and general performance measurements for this system operated with EMI-BF_4 are provided by Pettersson and Krejci [10, 11].

The experiments in this work were performed in the Turbovac vacuum test facility in the Space Propulsion Laboratory at MIT. Turbovac is evacuated by a mechanical pump and a turbomolecular pump to achieve a base pressure below 1E-6 Torr. As shown in Figure 4, the electrospray thruster was mounted on a rotational stage for testing such that it could be rotated for beam divergence measurements or aimed at different diagnostics without breaking

vacuum. An aluminum shield measuring 7 cm by 4 cm was mounted around the thruster to simulate a conductive spacecraft body. The shield, referred to herefter as the "spacecraft", had a cutout in its center, allowing it to be coplanar with the thruster's extractor grid.

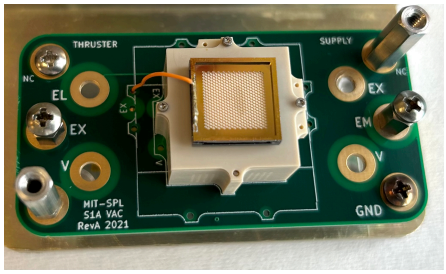

Fig. 3. iEPS unit mounted on a circuit board for laboratory testing.

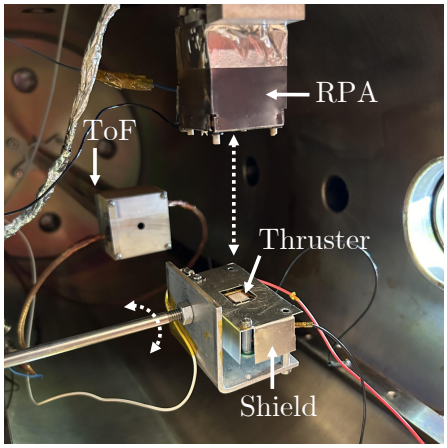

Fig. 4. Thruster, simulated spacecraft body, and diagnostics in Turbovac test facility.

High voltage is applied to the ionic liquid through a carbon xerogel distal electrode housed within the reservoir and to the extractor through a soldered connection. High voltage was supplied to the emitter and extractor electrodes using a Matsusada AP-3B1 fast high voltage amplifier with an output range of ±3 kV. The currents supplied to the emitter and extractor were measured using Analog Devices AD210AN isolation amplifiers. The spacecraft bias was applied using a Matsusada AMS-5B6 high voltage amplifier with an output range of ±5 kV.

Performance data were taken using the diagnostic instruments described in the following parts of this section. Each measurement was performed for spacecraft biases ranging from 0 V to ± 1000 V at increments of 100 V in both the positive and negative emission modes. All beam divergence and retarding potential analyzer measurements were repeated with the probe inlet located 5 cm (close) and 10 cm (far) from the thruster exit plane. Measurements were repeated at 0 V for each set of positive and negative spacecraft biases in case of drift in the thruster's behavior over time. The spacecraft bias was prescribed relative to the facility ground, which is emulating the true zero potential (labeled "Space GND" in Figure 2) in an on-orbit scenario, where true ground is usually related to the potential of ambient plasma or considered to be very far from the conductive body. In this work, the emitter and extractor potentials were also applied relative to the facility ground. However, it should be noted that in an on-orbit scenario these potentials would be referenced to that of the spacecraft, as shown in Figure 2. For each applied spacecraft bias V_{SC}, the extractor potential was held at −30 V relative to the spacecraft (to repel secondary electrons), and the emitter potential was manually adjusted in order to maintain a constant emitted current of about ±150 µA, replicating the scenario of an on-orbit thruster operating in a closed-loop current controlled mode. Note that although a range of spacecraft biases were intentionally examined here, in reality the potential to which a spacecraft charges with respect to space ground is generally not predictable or controllable for the architecture shown in Figure 2.

A retarding potential analyzer (RPA) measures the energy distribution of the thruster plume, which is used to estimate the energy efficiency and determine the effect of spacecraft charging on the energetic makeup of the emitted plume. The RPA is mounted on a linear stage located 10 cm above the thruster. As shown in Figure 5, the RPA consists of a plate with a circular aperture of 0.5 cm, a series of conductive grids, and a current collector, in that order. Particles in the thruster's plume first encounter a grounded grid, followed by three high-voltage grids to which the retarding potential V_{RP} is applied. Particles with kinetic energies less than qV_{RP} are repelled by the high voltage grids, while those with greater energies pass through. These particles encounter a second grounded grid and an electron suppression grid biased to −30 V before they are collected by a Faraday cup. To perform an RPA measurement, the thruster is aligned with the probe aperture and fired at a constant voltage V_0 while the retarding potential is swept between 0 and V_0 and the collector current is simultaneously recorded.

With the three high-voltage grids grounded, the RPA can be used to perform beam divergence measurements, which are used to determine the angular efficiency and return efficiency, as discussed in Section 5. The thruster was rotated to positive and negative angles with respect to the RPA until the measured current reached zero. The RPA was mounted on a linear stage, allowing for angular

scans to be taken between 5–10 cm from the thruster head. These measurements reveal the effect of spacecraft charging on the geometry of the thruster's plume.

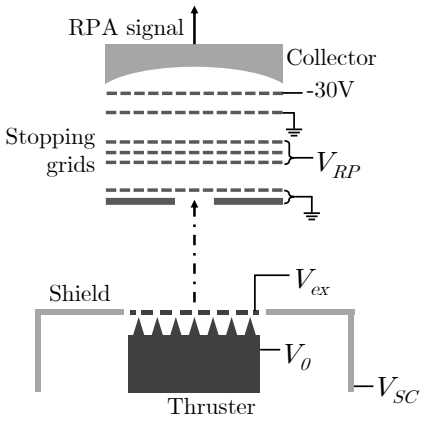

Fig. 5. Retarding potential analyzer diagram.

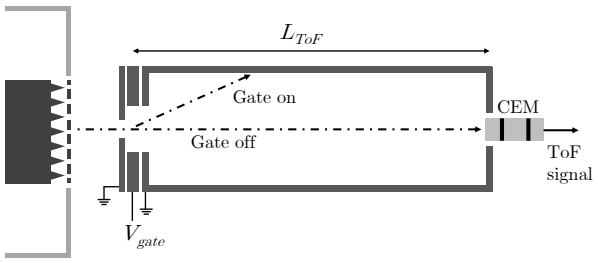

Fig. 6. Time-of-flight mass spectrometer diagram.

A custom-built linear time-of-flight (ToF) mass spectrometer was used to determine the velocity distribution of particles in the thruster's plume, allowing for the inference of performance metrics including thrust, mass flow rate, and specific impulse. The thruster is aimed at the instrument and fired at a constant emitter voltage V_0. A pair of electrodes form a deflection gate that is pulsed at a frequency of 100 Hz using a DEI PVM-210 pulse amplifier. When the gate is on, the electrodes are biased to 950 V and –950 V, creating a strong electric field that deflects the particles away from the time-of-flight detector. When the gate is off, the particles pass through the gate and traverse a field-free test section of a known length L_{ToF}. In the Turbovac chamber, L_{ToF} is 1.11 m. The output signal from the CEM is sent to a custom-built fast transimpedance amplifier before it is measured by an oscilloscope. It is important to note that the ToF deflection gate is located behind a grounded plate with an aperture of 0.5 cm in order to minimize variation in L_{ToF} from beam spreading. As such, only a small portion of the beam is able to reach the detector. Any spatial variations in plume composition that may exist are not considered in this work.

4. Results

The thruster was fired at a constant emitter current magnitude of 150 µA, as this is the nominal operating condition of the iEPS thruster. Extraction voltage was manually controlled to maintain this setpoint, with the test unit used in these experiments requiring approximately ±1050 V of extraction voltage to emit ±150 µA.

Figures 7 and 8 respectively give raw and normalized beam divergence measurements with the thruster firing at ±150 µA. Red curves show measurements for positive spacecraft biases, while blue curves show those for negative spacecraft biases, with lighter shades indicating greater spacecraft bias magnitudes. Solid lines represent measurements from the close probe position and dotted lines represent those from the far probe position. For clarity, measurements from each combination of spacecraft polarity and probe position are shown on a separate plot. Figure 8 shows normalized current profiles, where each curve is normalized relative to its own individual peak current in order to clearly illustrate the differences in the shapes of the beam profiles. In reality, the peak current measured by the Faraday cup changes with spacecraft bias, as illustrated in Figure 7. As expected, the current collected by the RPA approached zero as the spacecraft bias approached the extraction voltage, so only data for spacecraft biases up to ±800 V are shown and used in subsequent performance calculations. Each curve represents the average current measured at a given angle over at least four sweeps across the full range of angles. To compute the average, the angle domain was discretized into bins of 0.5 degree increments, and the mean of all current measurements recorded while the angle was within each bin is used to plot the average curves and to calculate all performance metrics.

Figure 7 shows the raw beam divergence measurements of current that reaches the RPA as a function of angle with respect to the thruster's geometric centerline. For cases in which the spacecraft and thruster are oppositely-biased (i.e. positive-mode emission where the spacecraft is negatively biased, or negative-mode emission where the spacecraft is positively biased), the emitted current that reaches the probe tends to zero as the spacecraft bias is increased, evidencing a return current that increases with spacecraft bias. The return current, which contributes no net thrust, constitutes a significant performance loss which will be discussed further in Section 5. When the spacecraft and thruster are biased in the same polarity (i.e. positive-mode emission where the spacecraft is positively biased, or negative-mode emission where the spacecraft is

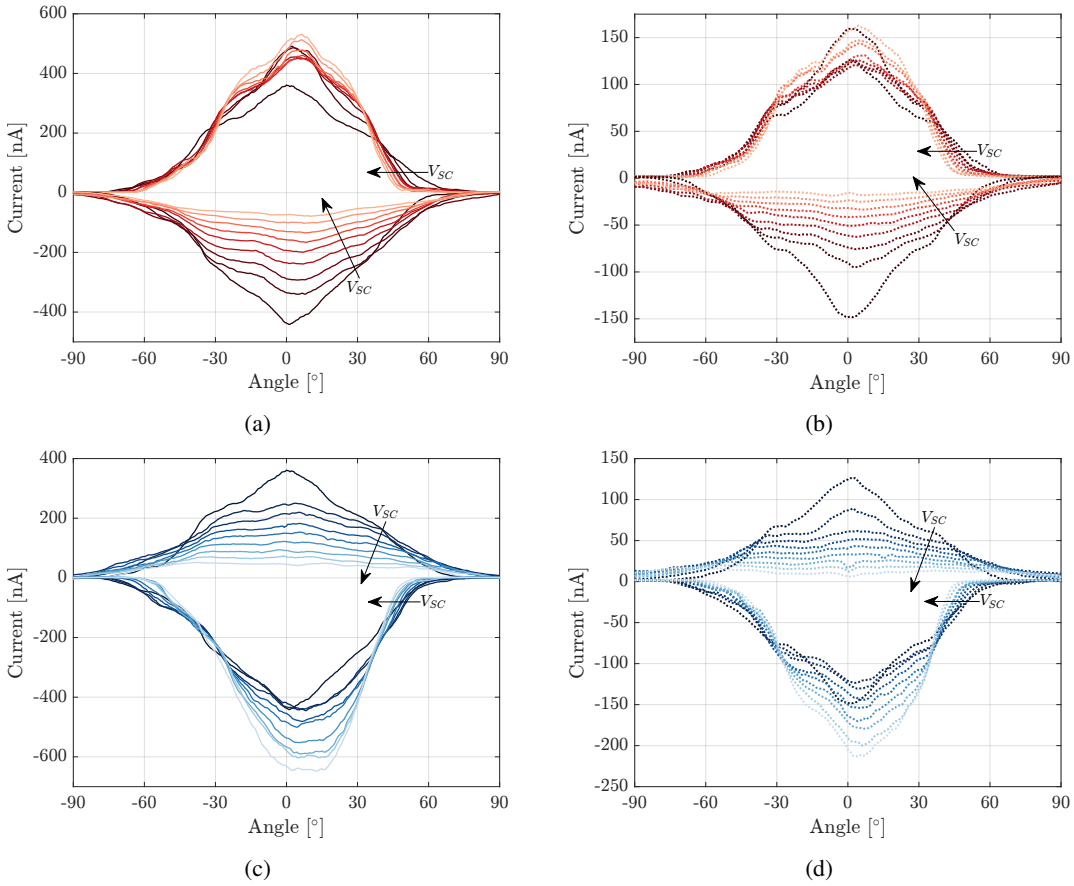

Fig. 7. Raw beam divergence measurements taken with the probe in the close (solid) and far (dashed) positions, for positive (red) and negative (blue) spacecraft biases. Arrows indicate increasing spacecraft bias.

negatively biased), the peak probe current increases with spacecraft potential while the current distribution is compressed.

Figure 8 shows normalized beam divergence measurements corresponding to the raw ones in Figure 7. For in cases in which the spacecraft and thruster are biased in opposite polarities, the current profiles show greater beam spreading with increasing spacecraft bias. Conversely, when the spacecraft and thruster are biased in the same polarity, the beam narrows with increasing spacecraft bias. These trends are seen in both the close and far probe measurements. However, the far probe measurements (Figures 8b and 8d) show greater beam spreading than the close probe measurements (Figures 8a and 8c) for the opposite-bias cases, indicating that the beam half-angle increases with distance from the thruster. This trend is a consequence of the spacecraft being oppositely charged, since the current profiles taken at 0 V spacecraft bias are nearly identical for the close and far probe cases. Greater beam spreading caused by interactions between the emitted particles and the spacecraft implies higher thrust losses, which will be discussed and calculated in Section 5.

The current profiles taken at zero spacecraft bias all show a primary peak located at the plume's centerline flanked by inflections at roughly ± 30 degrees, an unusual feature which has not been observed with similar thrusters [11, 12]. The inflections are likely a peculiarity in the emission characteristics of the particular iEPS thruster used in these experiments, since they did not appear in similar measurements taken with different thruster units. Another notable feature, shown in Figure 8d and to a lesser extent Figure 8b, is the tendency of the current profile to segment at very high opposite spacecraft biases. However, as shown in Figure 7, this segmentation is almost inconsequential since the net current being emitted at these high bias cases tends to zero.

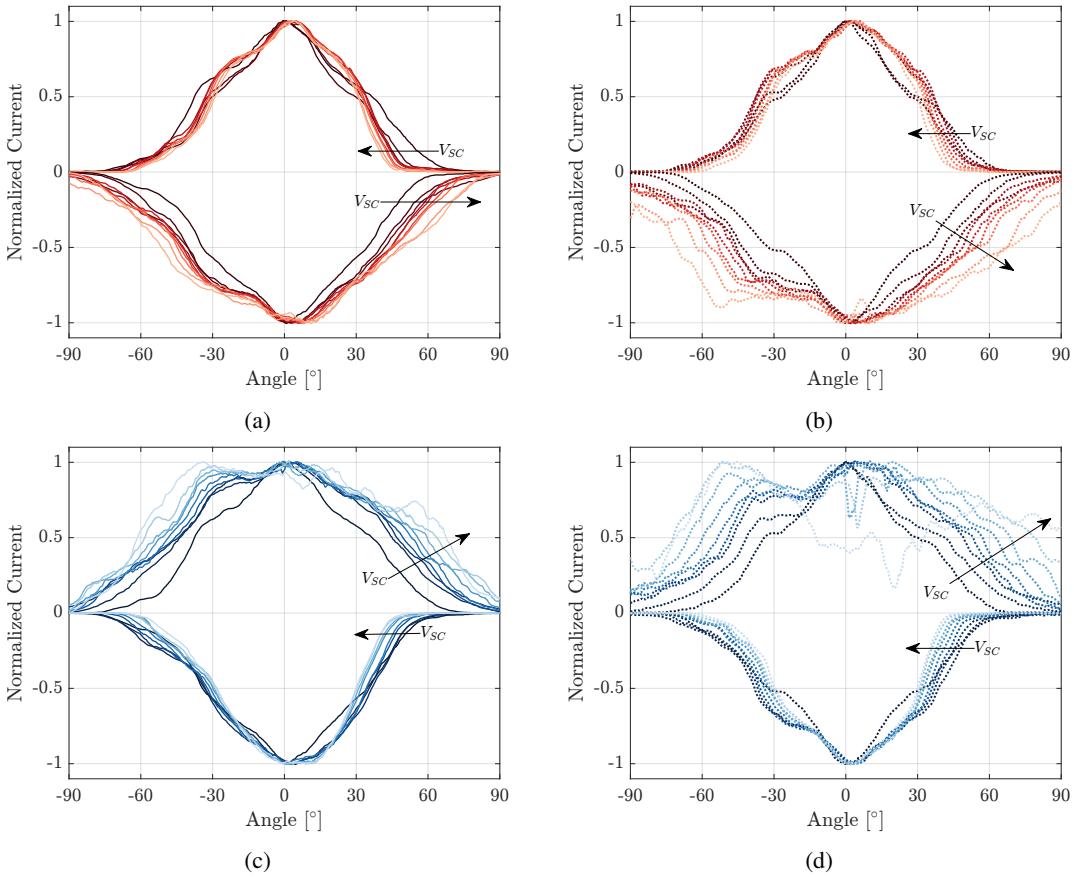

Fig. 8. Normalized beam divergence measurements taken with the probe in the close (solid) and far (dashed) positions, for positive (red) and negative (blue) spacecraft biases. Arrows indicate increasing spacecraft bias.

Figures 9a and 9b give RPA measurements with the thruster firing at $\pm 150\,\mu A$ for positive and negative spacecraft potentials, respectively. Lighter shades again indicate higher spacecraft bias magnitudes. Solid and dotted lines again represent measurements from the close and far probe positions, respectively. Retarding potential is normalized by the emitter potential relative to true ground for each measurement, which necessarily changes with spacecraft potential. Current is normalized by the peak current (i.e. the current measured when $V_{RP} \rightarrow 0$) for each scan individually. The magnitude of the current that reaches the RPA is not necessarily constant as spacecraft bias changes, as illustrated in Figure 15 provided in the Appendix, but normalizing each scan individually allows us to more easily identify differences in relative quantities between measurements. Like the beam divergence measurements, each RPA curve represents and average over at least four sweeps of the retarding potential. The RPA data were conditioned in the same way that was described for the beam divergence data, with each retarding potential domain discretized into 500 bins.

The RPA measurements taken at a spacecraft bias of 0 V show several key features that are normally used to identify different types of ions in the thruster's plume. The monoenergetic ion population has a stopping potential of V_0. Discrete signal steps indicate the breakup of an ion cluster in field-free space, and the corresponding normalized stopping potential is a known fraction of the mass of the fragmented ion to the parent ion. The most common of these events is the fragmentation of a dimer into a monomer and a neutral pair, which occurs at $V_{RP}/V_0 =$ 0.36 and 0.30 in the positive and negative modes, respectively. Sloped regions of the RPA curve indicate fragmentation that occurs in the acceleration region of the thruster, where the energy of the fragmented particle depends on its location within the potential field at the point of breakup [9].

For the case of positive mode emission where the spacecraft is positively charged, the most noticeable trend in the RPA measurements is the shift of the dimer frag-

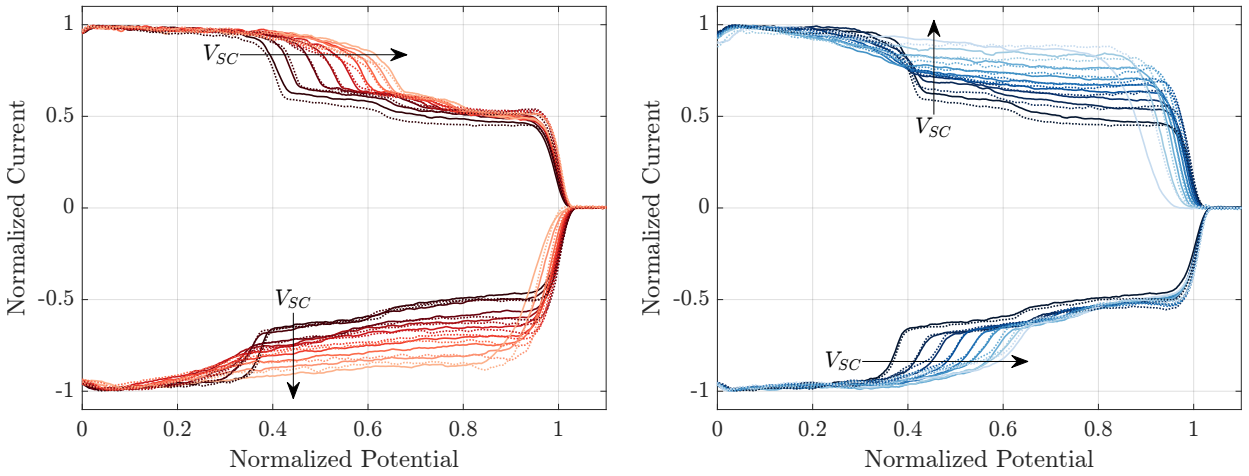

Fig. 9. RPA measurements taken in the close (solid) and far (dashed) probe positions for a) positive spacecraft biases, and b) negative spacecraft biases. Arrows indicate increasing spacecraft bias.

mentation step to higher normalized stopping potentials. Likely, monomers formed from the breakup events were repelled by the spacecraft electric field and accelerated to higher kinetic energies. The stopping potential in the case of a biased spacecraft therefore does not correspond to a predictable mass fraction of the parent ion. Additionally, the monomer step shows a broader distribution of particle energies as the spacecraft bias is increased. This is likely because the field-free fragmentation events occur at a range of distances from the thruster, resulting in the monomer fragments being accelerated to a range of terminal velocities. These trends are also seen for the case of negative mode emission with a negatively biased spacecraft, as shown in Figure 9b.

Figure 9a also shows RPA measurements for the case of negative mode emission where the spacecraft is positively biased. As the spacecraft bias is increased, there is a decrease in the relative abundance of parent dimers that have fragmented outside of the thruster as more of the monomers are attracted back to the spacecraft. The population of ions that reach the RPA therefore becomes increasingly monoenergetic with the spacecraft bias. However, it should be emphasized again that this current tends to zero, as shown in Figure 15. The same trend is observed in Figure 9b for the case of positive mode emission with a negatively biased spacecraft. Another notable trend in the opposite-bias RPA scans is the shifting of the location of the monoenergetic ion step to lower normalized potentials as the spacecraft bias is increased. Possibly, this may be attributed to ohmic losses in the ion extraction and emission process. While the absolute value of this loss should be independent of the spacecraft bias (so long as the extraction voltage is maintained), its ratio to the emitter potential (which decreases with V_{SC} in the opposite-bias case) increases. This trend therefore implies a decrease in energy efficiency with increasing spacecraft bias.

Unlike the RPA, the ToF instrument was not mounted on a movable stage, so measurements were collected at one fixed distance from the thruster and at all combinations of spacecraft and thruster polarity. The ToF curves for positive and negative spacecraft biases are given in Figure 10a and 10b, respectively. Much like the RPA measurements, the ToF signals have been normalized by their individual peak currents in order to clearly illustrate differences in relative abundances between measurements, if any such differences exist. Each ToF curve is an average of four measurements taken at identical conditions. The measurements taken at 0 V spacecraft bias reveal fairly typical beam compositions for the iEPS thruster operating with EMI-BF_4 propellant, where the beam is approximately an equal mixture of monomer and dimer ions, with heavier clusters and possibly liquid droplets making up a small percentage of the beam ($< 5\%$).

The key trend observed in all the ToF measurements is the changing of the terminal velocities of the groups of ion species resulting from increasing the magnitude of the potential of the spacecraft. For instance, we see for positive spacecraft bias cases that positive beams are overall accelerated and negative beams are overall decelerated as spacecraft bias is increased. In addition, for the case of a positive spacecraft and positive beam, increasing the spacecraft bias results in a segmentation of the current

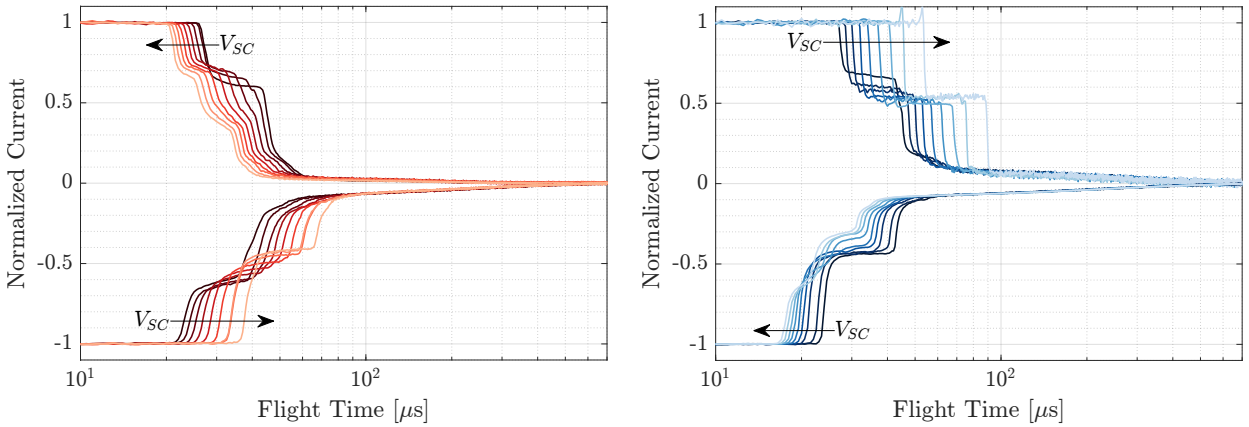

Fig. 10. Time-of-flight measurements for a) positive spacecraft biases, and b) negative spacecraft biases.

step associated with dimer species into two distinct steps: one corresponding to normal unfragmented dimers (that remained intact at least until they reached the field-free drift tube) and another corresponding to dimers that fragment into monomers outside of the thruster's acceleration region, a distinction that is not visible in ToF curves taken when the region outside the thruster is field free. These fragmented dimers are accelerated by the spacecraft bias to a larger extent due to their higher charge-to-mass ratio, and they therefore appear as a different species with terminal velocity between that of monomers and dimers. These same trends are observed in the negative spacecraft cases for negative ion beams. For the cases in which the spacecraft and emitter are biased in opposite polarities, we do not see evidence of fragmented dimers instead being decelerated by the spacecraft. Possibly, any monomers produced by these fragmentation events were attracted back to the spacecraft and thus were undetected in the time-of-flight measurements.

One less obvious trend observed in the ToF measurements is the tendency for the fraction of monomer species to increase with spacecraft bias for cases when the beam polarity is opposite that of the spacecraft. This trend can be seen in negative curves of Figure 10a where the monomer fraction gradually increases from just below to just above 50% as spacecraft bias is increased. Likewise, in the positive curves of Figure 10b the monomer fraction increases from approximately 40% to 50%. This change in plume composition would be consistent with more dimers being attracted back to the spacecraft as return current than monomers. Overall, the beam divergence measurements, energy spectra, and mass spectra presented in this section indicate that the spacecraft bias has a significant influence on the characteristics of the thruster plume.

5. Discussion

Thruster performance, including thrust and component efficiencies, can be calculated from the raw IV, beam divergence, RPA, and ToF data. All of these results are provided in Table 1 in the Appendix. The total efficiency η_T is the ratio of the beam's thrust power to the electric power supplied to the thruster. As given in Equation 2, the total efficiency is calculated from a number of component efficiencies that represent independent loss mechanisms measured in Section 4. This section will discuss each loss with emphasis on two that are expected to be most significantly influenced by spacecraft charging: the angular efficiency, η_θ, and the return efficiency, η_R, which will be defined later. Additional detail on the other components is provided in Refs. [2] and [11]. The ionization efficiency η_i is assumed to be 1 for these experiments.

$$\eta_T = \eta_{tr}^2 \eta_\theta \eta_E \eta_i \eta_p \eta_R^2 \quad [2]$$

The angular efficiency η_θ characterizes momentum lost to beam spreading. This loss can generally be substantial in electrospray thrusters, but is especially important in cases where there is spacecraft charging due to potential interactions between the spacecraft electric field and the ion beam geometry. The angular efficiency is calculated using Equation 3 [12], assuming particles are emitted with the same velocity at all angles. Here, $I(\theta)$ is the angular current profile and θ is the angle between the centerlines of the thruster and the RPA. θ_c is the central angle of the beam, defined as the angle at which the integrated currents on either side are equal, and is calculated using Equation 4. θ_c was subtracted from the values of θ prior to calculating the angular efficiency. Note that integration bounds of $\pm\pi$ are used in Equation 3 to account for probe cur-

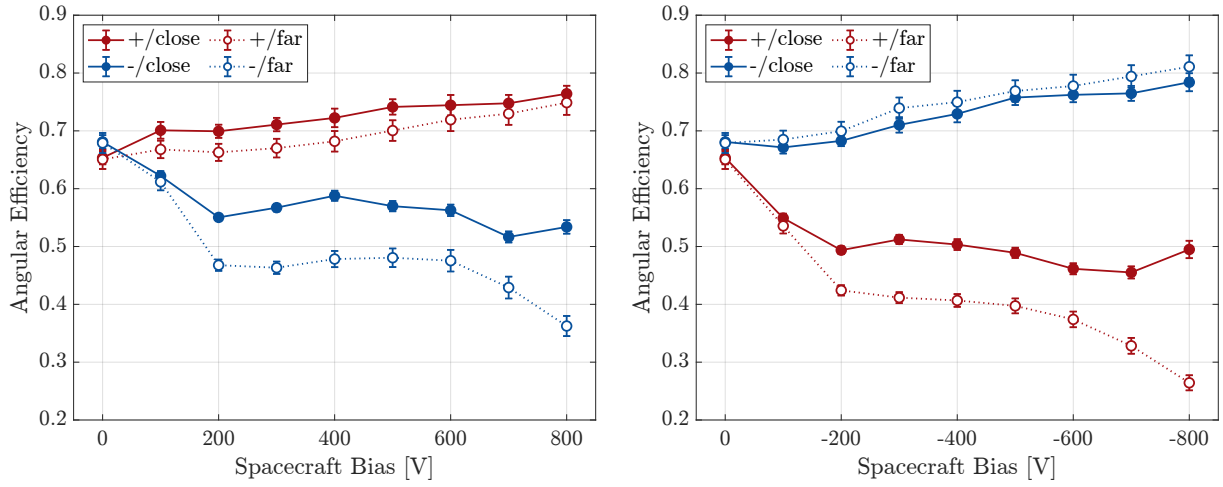

(a) (b)

Fig. 11. Angular efficiency for a) positive spacecraft biases, and b) negative spacecraft biases.

rent being measured at angles greater than ±90 degrees in some cases where the spacecraft and plume were oppositely biased. The sign convention used here ensures that any current measured at $|\theta| > 90°$ diminishes the angular efficiency, since particles with such trajectories would generate a negative thrust on the spacecraft.

$$\eta_\theta = \left[\frac{\int_{-\pi}^{\pi} I(\theta) \cos\theta \sin|\theta| d\theta}{\int_{-\pi}^{\pi} I(\theta) \sin|\theta| d\theta} \right]^2 \quad [3]$$

$$\int_{-\pi}^{\theta_c} I(\theta) d\theta = \int_{\theta_c}^{\pi} I(\theta) d\theta \quad [4]$$

Figures 11a and 11b show the calculated angular efficiencies for positive and negative spacecraft biases respectively and all combinations of emission polarity and probe position. Uncertainty was estimated by considering the noise of the signal itself and the repeatability of the measurement over multiple trials. Error bars represent 3σ uncertainty, as calculated by propagating the uncertainty associated with each data point in the raw data through the calculation of angular efficiency. It is important to note that not all sources of experimental error could be directly accounted for, especially any systematic error or more complex forms of random error. At a spacecraft bias of 0 V, the angular efficiencies in the positive and negative modes are about 0.67 and 0.69 respectively, and are fairly close between the close and far probe positions. When the spacecraft and ion beam are the same polarity, the angular efficiency increases steadily with spacecraft bias. This trend is reflected in the beam profiles shown in Figure 8, which show the beam narrowing as the spacecraft bias is increased. For cases in which the spacecraft and ion beam are opposite polarities, the converse trend is observed, where the angular efficiency decreases with spacecraft bias. This decrease is greater than the corresponding increase in efficiency for the like-bias cases, meaning that a net momentum loss results from spacecraft charging.

Also noteworthy in Figure 11 is the difference between the close and far probe efficiencies in the opposite-bias cases, with the far probe efficiencies consistently lower than the close probe efficiencies. This trend was anticipated from Figure 8, which showed increased beam spreading measured in the far probe position. Interestingly, the greatest decrease in efficiency, especially for the far probe data, is seen within relatively low spacecraft biases of just ±200 V. That the measured beam divergence is seen to change with probe position raises the question of what the true (i.e. performance-determining) plume structure and corresponding angular efficiency are in the space environment. The ability to take representative measurements thereof is naturally limited in any vacuum test facility due to the influence of the grounded chamber body on the plume structure. As such, it is suggested that future studies use a computational approach to more closely study electrospray plume evolution in spacecraft charging environments. In the scope of this work, however, subsequent performance calculations will utilize the angular efficiencies derived from our far probe measurements.

Now, we will define the return efficiency η_R, which accounts for thrust lost due to return current. Note that η_R should generally be 1 unless there is spacecraft charging or another process that causes emitted ions to be attracted

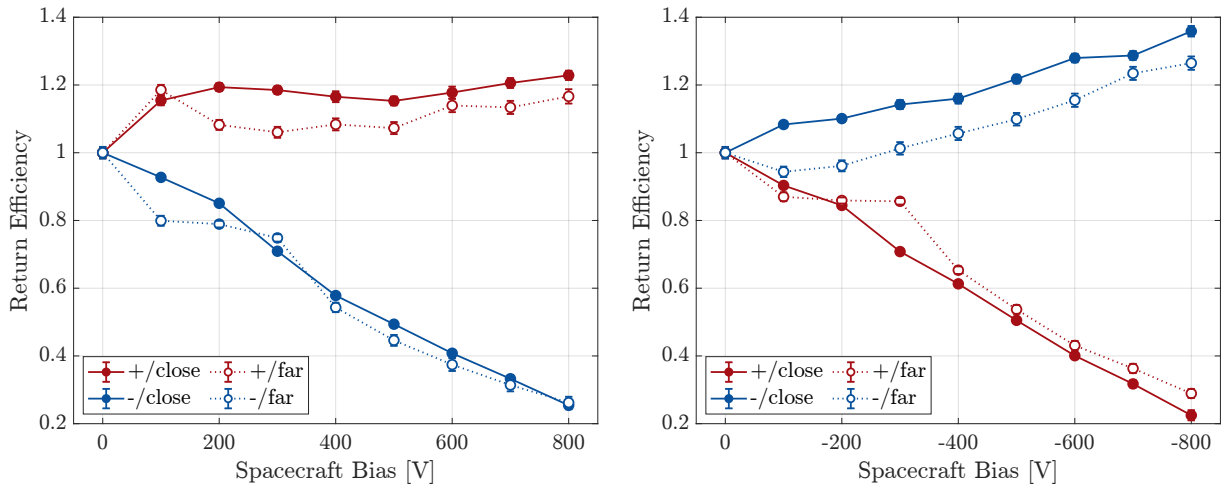

Fig. 12. Return efficiency for a) positive spacecraft biases, and b) negative spacecraft biases.

back to the spacecraft. As given in Equation 5, we can calculate η_R as the ratio of net emitted current when the spacecraft is biased (I_*) to that when the spacecraft is not biased (I) with respect to true ground. $I_*(\theta)$ and $I(\theta)$ are obtained from the beam profile measurements presented in Section 7. Figures 12a and 12b show η_R plotted as a function of spacecraft bias for positively and negatively biased spacecraft, respectively, with measurements provided for both positive and negative emission modes and for the close and far probe positions. Uncertainty is estimated in the same way that is described for angular efficiency.

$$\eta_R = \frac{\int_{-\pi}^{\pi} I_*(\theta) d\theta}{\int_{-\pi}^{\pi} I(\theta) d\theta} \quad [5]$$

As expected, the return efficiency tends to decrease with increasing spacecraft bias for the cases in which the spacecraft and ion beam are opposite in polarity. This loss is significant, reaching about 50% at moderate spacecraft potentials of 500 V. The opposite-bias efficiencies for the close and far probe measurements are quite close, indicating that the length scale over which particles decelerate and return to the spacecraft may be much smaller than the probe distances used in these experiments.

A questionable observation is the return efficiency increasing beyond 1 for the cases in which the spacecraft and ion beam are the same polarity. Of course, this is not truly possible if the emitted current is fixed. The likely reason for this is the assumption behind Equation 5 that the beam had an axisymmetric current distribution, and that the 1-D angular current sweep performed was representative of any given cross section of the plume. Any asymmetries in the electric field geometry in our setup, had they existed, could have disproportionately directed current along the direction of the angular sweep such that more total current reached the RPA when the spacecraft was biased.

The transmission efficiency, η_{tr}, accounts for any current that impinges on the extractor grid rather than passing through an aperture, and thus does not contribute to thrust. It is calculated according to Equation 6, where I_{em} is the total current through the emitter and I_{ex} is the intercepted current. I_{em} and I_{ex} were averaged over all periods during the test where the thruster was firing in steady state at an emitted current magnitude of 150 µA and the spacecraft was not biased. When the spacecraft was biased, it was not possible to distinguish between true intercepted current and current that returned to the extractor after being emitted. We therefore assume the transmission efficiency was constant and independent of the spacecraft potential, which is a reasonable assumption since the emitted current and extraction voltage were approximately constant over all conditions tested. The transmission efficiency was determined to be 0.99 in the positive mode and 0.98 in the negative mode.

$$\eta_{tr} = \frac{I_{em} - I_{ex}}{I_{em}} \quad [6]$$

The energy efficiency η_E characterizes energy lost during the ion emission and extraction process, and is defined as the ratio of the true beam potential to the applied emitter potential. The beam potential is taken to be the RPA stopping potential that corresponds to the highest peak of

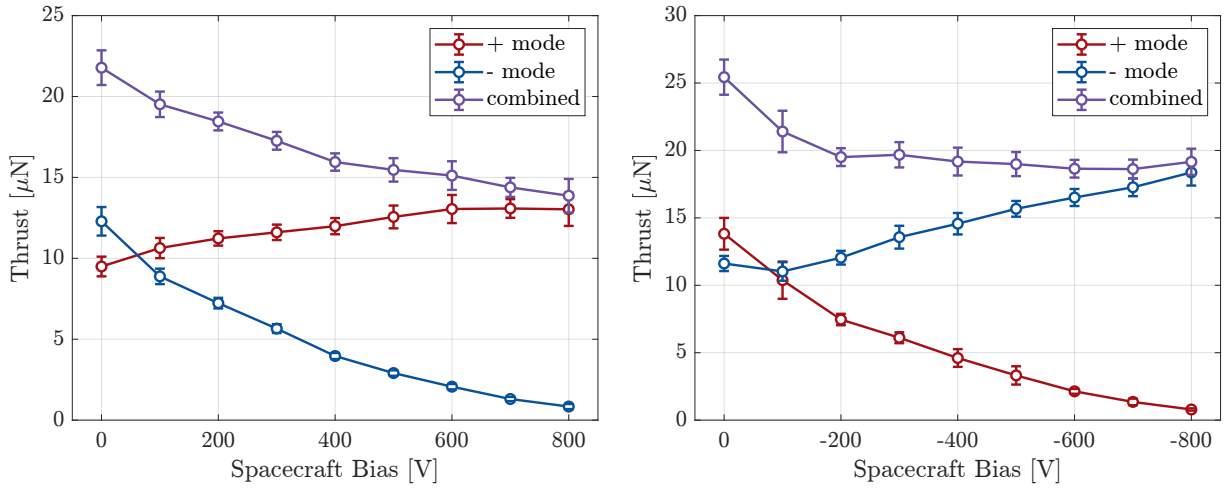

Fig. 13. Corrected thrust for a) positive spacecraft biases, and b) negative spacecraft biases.

the ion energy spectrum. Because the monoenergetic current step (generally the largest and steepest step in an RPA signal) is not perfectly vertical in real data, the approximate start and end of the this step are determined by numerically detecting deviations in the average value of the signal, and we define the precise location of this step and thus the peak of the energy spectrum to be the normalized stopping potential at which the current decreases below 90% of its value prior to the start of the step. All energy efficiencies are reported in Table 1. For cases in which the spacecraft and ion beam are opposite polarities, η_E decreases somewhat with increasing spacecraft bias, but by less than 0.1 in all cases. As discussed previously, the likely cause for this is ohmic losses during the ion emission process. When the spacecraft and beam are the same polarity, the energy efficiency remains close to 1 in all cases.

The polydispersive efficiency η_p accounts for power wasted by accelerating particles of varying specific charge through a potential difference. It can be calculated from ToF-based performance measurements as the ratio of jet power, $\frac{1}{2}F_{ToF}^2/\dot{m}_{ToF}$, to input electric power, $I_{em}V_0$, as given in Equation 7. All polydispersive efficiencies are provided in Table 1.

$$\eta_p = \frac{F_{ToF}^2/2\dot{m}_{ToF}}{I_{em}V_0} \quad [7]$$

Thrust is estimated from ToF measurements using Equation 8, where V_0 is the applied emitter potential, L_{ToF} is the field-free drift distance, I_{em} is the total emitted current, and $\bar{I}(t)$ is the time-of-flight signal normalized by its individual maximum current. Similarly, the mass flow rate is calculated using Equation 9. It should be noted that there are inherent limitations to using indirect methods like ToF to determine true performance. However, ToF is typically more practical than direct methods for capturing performance trends, and tends to show close qualitative agreement with direct methods once key loss mechanisms have been properly accounted for [13, 14].

$$F_{ToF} = \frac{2V_0}{L_{ToF}} I_{em} \int_0^\infty \bar{I}(t)dt \quad [8]$$

$$\dot{m}_{ToF} = \frac{4V_0}{L_{ToF}^2} I_{em} \int_0^\infty t\bar{I}(t)dt \quad [9]$$

Figures 13a and 13b show thrust plotted as a function of spacecraft bias for positively and negatively biased spacecraft, respectively. Positive and negative mode thrust are shown separately and combined, with the intention of the combined thrust representing the performance from a pair of electrospray thrusters operated together in a dual-polarity pair on a charged spacecraft. These thrust values have been corrected for energy, transmission, angular, and return losses according to $F = \eta_{tr}\eta_E\eta_R\sqrt{\eta_\theta}F_{ToF}$. We used values of η_E, η_R, and η_θ calculated from far probe measurements, and set any $\eta_R > 1$ to 1. Uncertainty is estimated by propagating the 3σ uncertainty calculated for each component efficiency through the calculation of F. We note again that only uncertainty associated with measurement noise and repeatability are considered here. The thrust at zero spacecraft bias is close between the positive and negative modes. For positive

spacecraft biases, the thrust produced in the positive mode increases as a function of spacecraft bias, primarily due to the particles being accelerated by the spacecraft but also because of an improvement in the angular efficiency, as shown in Figure 11a. Meanwhile, the negative-mode thrust decreases substantially as a function of spacecraft bias due to the combined effects of the increasing return current, beam divergence, and the spacecraft decelerating emitted particles. The increase in positive-mode thrust is insufficient to counteract the decrease in negative-mode thrust, resulting in a decrease in combined thrust with increasing spacecraft bias. The combined thrust penalty is about 36% at $V_{SC} = 800$ V. Analogous trends are seen in Figure 13b for the case of the negatively biased spacecraft, with a thrust penalty of about 25% at $V_{SC} = -800$ V. Overall, these results show that irrespective of the spacecraft polarity, a pair of electrospray thrusters operated in the dual-polarity will generally produce less total thrust in a spacecraft charging scenario.

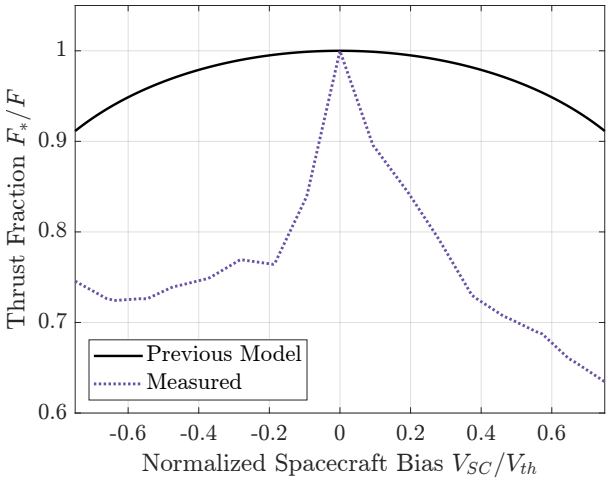

Fig. 14. Fractional thrust predicted by Equation 1 [5] and experimentally measured here (corrected for all efficiencies)

Recall Equation 1, presented by Mier-Hicks [5] to estimate the thrust fraction F_*/F (i.e. ratio of thrust produced for a charged spacecraft to that when the spacecraft is non-charged) for a dual-polarity pair of electrospray thrusters as a function of normalized spacecraft bias V_{SC}/V_{th} (i.e. ratio of the spacecraft bias to the extraction voltage). This model predicts a square root dependence of the thrust fraction on V_{SC}/V_{th}. As such, even in the worst-case scenario where the spacecraft charges fully to one of the thruster's extraction voltages, the thrust penalty should be just 30%, with minimal losses at moderate spacecraft biases. Figure 14 shows this predicted thrust fraction against that which was determined experimentally here. The experimental thrust fraction is defined as the combined corrected thrust normalized by its value at zero spacecraft bias, and was linearly interpolated between setpoints of V_{SC}/V_{th}. In contrast to Mier-Hicks' prediction, our results show that even low levels of spacecraft charging can result in substantial thrust loss. The discrepancy can be explained by performance losses not considered in the model, primarily beam divergence and return current.

Other key performance metrics, including the mass flow rate and specific impulse, are provided in Table 1. The mass flow rate in this work is defined as the rate of propellant consumption rather than the rate of mass leaving the spacecraft (since, in some cases, particles returned to the spacecraft after being emitted). As such, the mass flow rates were corrected only for energy efficiency losses according to $\dot{m} = (\eta_E/\eta_i)\dot{m}_{ToF}$. The mass flow rates for the biased spacecraft cases were assumed to be equal to those in the corresponding emission mode when the spacecraft was not biased. The specific impulse, defined as the impulse delivered to the spacecraft by the thruster per unit weight of propellant, is then calculated from the corrected thrust and mass flow rate according to Equation 10, where g_0 is the standard acceleration due to gravity. As expected, Table 1 shows that the specific impulse tends to zero when the spacecraft and beam are opposite polarities due to the decrease in thrust.

$$I_{sp} = \frac{F}{g_0 \dot{m}} \quad [10]$$

The results presented here demonstrate that spacecraft charging is an important consideration when flying electrospray propulsion systems, since, in contrast to previous hypotheses, even relatively low levels of charging can have an appreciable impact on thruster performance. Therefore, expansion on this work is merited as there are additional physical considerations that may be relevant and diverse electrospray architectures for which the impact to performance may be very different. As an example of the former, our thrust and efficiency calculations did not account for spatial variations in particle velocity or mass across the plume. Such variations, which have been observed in electrospray thrusters [15, 16], could potentially be affected by spacecraft charging and thus have a reciprocal effect on thruster performance. Regarding the latter, it could be useful to determine how performance is affected by the relative scale of the spacecraft and parameters of the propulsion system (such as the number, polarities, and spatial arrangement of individual thrusters).

6. Conclusions

Spacecraft charging is an undesirable but common phenomenon for both Earth-orbiting and deep-space satellites in which a spacecraft accumulates charge, increasing or decreasing its electric potential with respect to its surroundings or different parts of the vehicle. Previous work has examined the nuanced process by which electrospray thrusters operated in dual-polarity pairs can induce significant levels of spacecraft charging. This work aimed to characterize the physical interactions between a charged spacecraft and an electrospray thruster plume and quantify the resulting impacts to the thruster's performance.

The performance of an MIT iEPS electrospray thruster was measured in a simulated spacecraft charging environment using a biased conductive shield to mimic a charged spacecraft body. Beam divergence measurements, energy spectra, and mass spectra were obtained at applied spacecraft potentials ranging from zero volts to the thruster's extraction voltage. When the spacecraft and thruster plume are of the same polarity, the system's thrust output and component efficiencies tend to increase with spacecraft bias as the emitter is floated at higher voltages with respect to space ground. Meanwhile, when the spacecraft and plume are opposite in polarity, the performance decreases at higher spacecraft biases, primarily due to an increase in beam divergence and return current. For a pair of thrusters operated in the dual-polarity configuration, the decrease in thrust output from one thruster outweighs the increased thrust produced by the other, resulting in a net thrust reduction with increasing spacecraft bias regardless of the polarity in which the spacecraft is charged. This thrust penalty can be significant at fairly low spacecraft biases. Overall, the results of this work provide a more complete picture of in-space electrospray performance and serve to highlight the importance of establishing a proper neutralization system for electrospray-propelled spacecraft.

Appendix

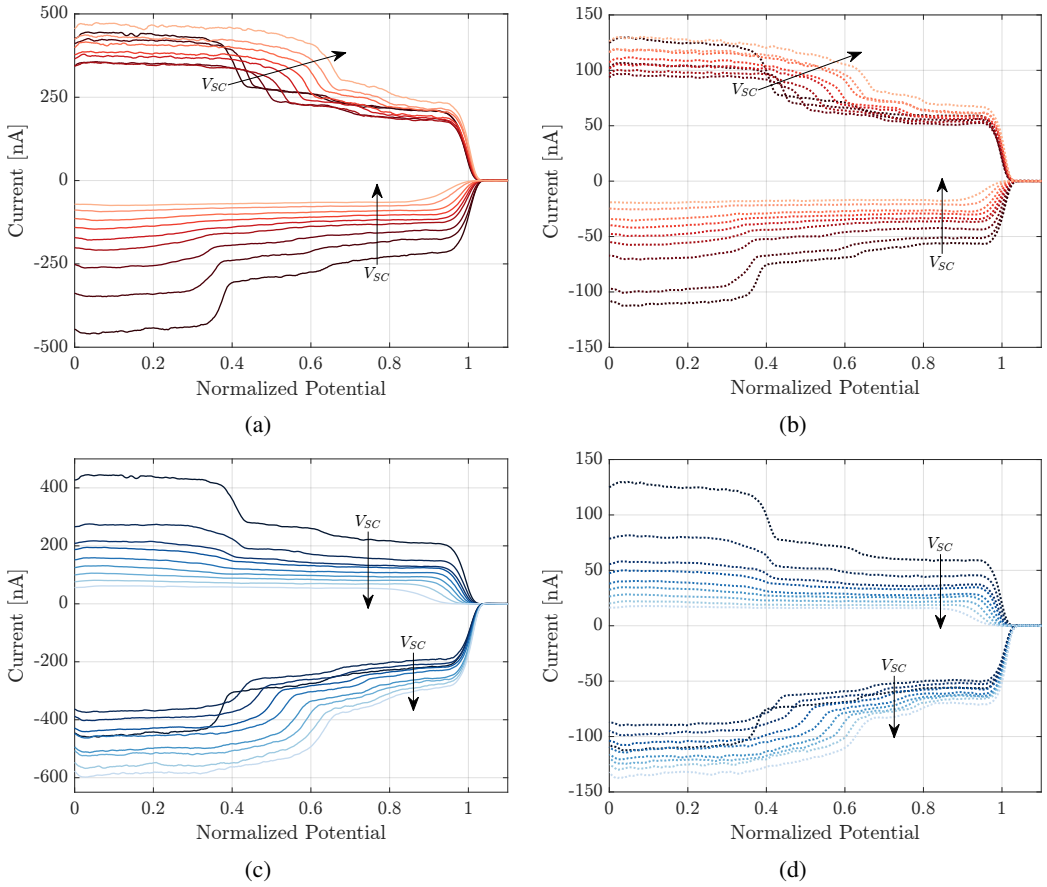

Fig. 15. Raw RPA measurements taken with the probe in the close (solid) and far (dashed) positions, for positive (red) and negative (blue) spacecraft biases. Arrows indicate increasing spacecraft bias.

V_{SC} [V]	Emission Mode	η_{tr}	η_θ	η_E	η_R	η_p	η_T	F [µN]	$\dot{m}$ [µg/s]	I_{sp} [s]
0	+	0.99	0.65	0.97	1.00	0.77	0.47	9.40	0.59	1621
100	+	0.99	0.67	0.98	1.00	0.66	0.42	10.53	0.59	1816
200	+	0.99	0.66	0.98	1.00	0.58	0.37	11.12	0.59	1918
300	+	0.99	0.67	0.98	1.00	0.62	0.40	11.49	0.59	1982
400	+	0.99	0.68	0.98	1.00	0.61	0.40	11.87	0.59	2047
500	+	0.99	0.70	0.99	1.00	0.49	0.33	12.43	0.59	2145
600	+	0.99	0.72	0.99	1.00	0.61	0.42	12.92	0.59	2228
700	+	0.99	0.73	0.99	1.00	0.62	0.44	12.95	0.59	2234
800	+	0.99	0.75	0.99	1.00	0.59	0.43	12.90	0.59	2225
0	-	0.98	0.68	0.98	1.00	0.30	0.20	12.04	2.37	519
100	-	0.98	0.61	0.98	0.80	0.32	0.12	8.71	2.37	375
200	-	0.98	0.47	0.98	0.79	0.34	0.10	7.08	2.37	305
300	-	0.98	0.46	0.97	0.75	0.36	0.09	5.54	2.37	239
400	-	0.98	0.48	0.97	0.54	0.39	0.05	3.88	2.37	167
500	-	0.98	0.48	0.97	0.45	0.41	0.04	2.85	2.37	123
600	-	0.98	0.48	0.96	0.37	0.44	0.03	2.03	2.37	87
700	-	0.98	0.43	0.95	0.31	0.47	0.02	1.28	2.37	55
800	-	0.98	0.36	0.93	0.26	0.56	0.01	0.82	2.37	35
0	+	0.99	0.65	0.97	1.00	0.34	0.21	13.68	2.76	506
-100	+	0.99	0.54	0.97	0.87	0.30	0.11	10.27	2.76	380
-200	+	0.99	0.42	0.97	0.86	0.37	0.11	7.39	2.76	273
-300	+	0.99	0.41	0.97	0.86	0.34	0.09	6.05	2.76	224
-400	+	0.99	0.41	0.96	0.65	0.38	0.06	4.56	2.76	169
-500	+	0.99	0.40	0.95	0.54	0.39	0.04	3.28	2.76	121
-600	+	0.99	0.37	0.95	0.43	0.49	0.03	2.11	2.76	78
-700	+	0.99	0.33	0.93	0.36	0.62	0.02	1.34	2.76	49
-800	+	0.99	0.26	0.89	0.29	0.65	0.01	0.78	2.76	29
0	-	0.98	0.68	0.98	1.00	0.30	0.20	11.38	2.22	522
-100	-	0.98	0.68	0.98	0.94	0.27	0.16	10.81	2.22	495
-200	-	0.98	0.70	0.99	0.96	0.26	0.17	11.80	2.22	541
-300	-	0.98	0.74	0.99	1.00	0.25	0.18	13.30	2.22	610
-400	-	0.98	0.75	0.99	1.00	0.25	0.18	14.28	2.22	654
-500	-	0.98	0.77	0.99	1.00	0.23	0.17	15.36	2.22	704
-600	-	0.98	0.78	0.99	1.00	0.22	0.17	16.18	2.22	742
-700	-	0.98	0.79	0.99	1.00	0.22	0.17	16.92	2.22	776
-800	-	0.98	0.81	1.00	1.00	0.21	0.17	18.00	2.22	825

Table 1. Performance results for each spacecraft bias, including component efficiencies, corrected thrust, mass flow rate, and specific impulse.

References

[1] P. C. Lozano, B. L. Wardle, P. Moloney, and S. Rawal, "Nanoengineered thrusters for the next giant leap in space exploration," *Mrs Bulletin*, vol. 40, no. 10, pp. 842–849, 2015.

[2] P. Lozano and M. Martínez-Sánchez, "Ionic liquid ion sources: Suppression of electrochemical reactions using voltage alternation," *Journal of colloid and interface science*, vol. 280, no. 1, pp. 149–154, 2004.

[3] N. Demmons, J. Knott, T. Fedkiw, and N. Alvarez, "Qualification of the bet-max electrospray propulsion system," in *37th International Electric Propulsion Conference*, Cambridge, Massachusetts, USA, Jun. 2022.

[4] S. Z. Shaik, "Single-polarity ion electrospray propulsion," M.S. thesis, Massachusetts Institute of Technology, 2023.

[5] F. Mier-Hicks and P. C. Lozano, "Spacecraft-charging characteristics induced by the operation of electrospray thrusters," *Journal of Propulsion and Power*, vol. 33, no. 2, pp. 456–467, 2017.

[6] S. T. Lai and K. Cahoy, *Spacecraft Charging*. CRC Press, 2016, ch. S1200536440000.

[7] F. Mier Hicks, "Spacecraft charging and attitude control characterization of electrospray thrusters on a magnetically levitated testbed," Ph.D. dissertation, Massachusetts Institute of Technology, 2017.

[8] D. G. Courtney, H. Shea, K. Dannenmayer, and A. Bulit, "Charge neutralization and direct thrust measurements from bipolar pairs of ionic electrospray thrusters," *Journal of Spacecraft and Rockets*, vol. 55, no. 1, pp. 54–65, 2018.

[9] C. E. Miller, "Characterization of ion cluster fragmentation in ionic liquid ion sources," Ph.D. dissertation, Massachusetts Institute of Technology, 2019.

[10] G. M. Pettersson, A. R. Bruno, M. N. Corrado, B. S. Medina, D. Krejci, and P. C. Lozano, "Performance measurement and propellant testing for the step-1 cubesat elecrospray thrusters," *International Electric Propulsion Conference*, 2022.

[11] D. Krejci, F. Mier-Hicks, R. Thomas, T. Haag, and P. Lozano, "Emission characteristics of passively fed electrospray microthrusters with propellant reservoirs," *Journal of Spacecraft and Rockets*, vol. 54, no. 2, pp. 447–458, 2017.

[12] E. Petro, A. Bruno, P. Lozano, L. E. Perna, and D. Freeman, "Characterization of the tile electrospray emitters," in *Aiaa propulsion and energy 2020 forum*, 2020, p. 3612.

[13] D. G. Courtney, S. Dandavino, and H. Shea, "Comparing direct and indirect thrust measurements from passively fed ionic electrospray thrusters," *Journal of Propulsion and Power*, vol. 32, no. 2, pp. 392–407, 2016.

[14] M. N. Corrado, A. Bruno, and P. Lozano, "Direct and indirect thrust measurements of ionic-liquid electrospray thrusters on a magnetically-levitated testbed," in *AIAA SCITECH 2024 Forum*, 2024, p. 1344.

[15] M. Davis, A. L. Collins, and R. E. Wirz, "Electrospray plume evolution via discrete simulations," in *Proceedings of the 36th International Electric Propulsion Conference, IEPC-2019, Vienna, Austria*, vol. 590, 2019.

[16] M. Schroeder, X. Gallud Cidoncha, A. Bruno, O. Jia-Richards, and P. Lozano, "Angular properties of ionic liquid electrospray emitters," in *AIAA SCITECH 2023 Forum*, 2023, p. 1408.